Interpretation®

MECHANISMS OF OVERBURDEN DEFORMATION ASSOCIATED WITH THE EMPLACEMENT OF THE TULIPAN SILL, MID-NORWEGIAN MARGIN

Journal:	*Interpretation*
Manuscript ID	INT-2016-0155
Manuscript Type:	2015-12 Subsurface expression of igneous systems and their impacts on petroleum systems
Date Submitted by the Author:	28-Sep-2016
Complete List of Authors:	Schmiedel, Tobias; Universitetet i Oslo Det Matematisk-naturvitenskapelige Fakultet, Department of Geosciences Kjoberg, Sigurd; Universitetet i Oslo Det Matematisk-naturvitenskapelige Fakultet, Department of Geosciences Planke, Sverre; Volcanic Basin Petroleum Research AS Magee, Craig; Imperial College, Earth Science and Engineering Galland, Olivier; Universitetet i Oslo Det Matematisk-naturvitenskapelige Fakultet, Department of Geosciences Schofield, Nick; University of Aberdeen, Department of Geology and Petroleum Geology Jackson, Christopher; Imperial College, Earth Science & Engineering
Keywords:	3D, interpretation, volcanics, Europe
Subject Areas:	Case studies

SCHOLARONE™
Manuscripts

MECHANISMS OF OVERBURDEN DEFORMATION ASSOCIATED WITH THE EMPLACEMENT OF THE TULIPAN SILL, MID-NORWEGIAN MARGIN

Tobias Schmiedel[1], Sigurd Kjoberg[2], Sverre Planke[2, 3], Craig Magee[4], Olivier Galland[1],
Nick Schofield[5], and Christopher A-L Jackson[4]

[1]*Physics of Geological Processes (PGP), Department of Geosciences, University of Oslo, Blindern, Postbox 1048, 0316 Oslo, NORWAY, tobias.schmiedel@geo.uio.no / olivier.galland@geo.uio.no*

[2]*Centre for Earth Evolution and Dynamics (CEED), Department of Geosciences, Postbox 1028, Blindern, N-0315 Oslo, NORWAY, planke@vbpr.no / sigurd.kjoberg@geo.uio.no*

[3]*Volcanic Basin Petroleum Research AS (VBPR), 0349 Oslo, NORWAY*

[4]*Basins Research Group, Department of Earth Science and Engineering, Imperial College London, London SW7 2BP, UK, c.magee@imperial.ac.uk / c.jackson@imperial.ac.uk*

[5]*Department of Geology and Petroleum Geology, School of Geosciences, University of Aberdeen, Meston Building, Old Aberdeen, Aberdeen AB24 3UE, UK, n.schofield@abdn.ac.uk*

Original paper date of submission: 27.09.2016

Revised paper date of submission: ----

For Peer Review

ABSTRACT

Accounting for igneous intrusions into sedimentary basins is important to the petroleum industry because magmatism deforms the host rock and affects the thermal evolution of a basin, thereby influencing hydrocarbon generation, migration, and accumulation. Presently, numerous mechanisms concerning the syn-emplacement (i.e. elastic bending related active uplift and aureole induced volume reduction) and post-emplacement (i.e. differential compaction) deformation of the host rock have been suggested. In this study, we investigate the relevance of the different existing syn- or post-emplacement related mechanical models of dome growth accommodating the emplacement of igneous sills. We use high-quality 3D seismic and well data located in the western part of the Møre Basin (mid-Norwegian margin) to analyze the deformation of Cretaceous – Paleogene overburden associated with the emplacement of the Tulipan saucer-shaped sill between 55.8 and 54.9 Ma. Horizon interpretations and various thickness and attribute maps show a clear correlation between the saucer-shaped Tulipan sill and an observed domed structure above. Additionally, we observe in the shallow parts of the dome structure hydrothermal vent complexes connected by fractures only along the periphery of the underlying sill. We show that the Tulipan sill is responsible for the dome structure in the overburden of the study area. At the same time we see that not solely one of the different mechanisms of overburden deformation can be responsible for the observed dome structure, but the combination of them.

For Peer Review

INTRODUCTION

Volcanic basins contain significant volumes of igneous rocks (Planke et al., 2005) and are explored for hydrocarbons all over the world, both onshore and offshore; e.g., the Rockall Basin (e.g., Magee et al., 2014), the Faroe-Shetland Basin (e.g., Smallwood and Maresh, 2002), the Møre and Vøring basins (e.g., Planke et al., 2005; Cartwright and Hansen, 2006) the Karoo Basin (e.g., Svensen et al., 2012), and the Neuquén Basin (e.g., Kay et al., 2006). The magma plumbing systems in these basins are primarily dominated by interconnected networks of sill intrusions, the emplacement of which can significantly deform the host rock and potentially influence petroleum system development (Kontorovich et al., 1997; Thomson and Hutton, 2004; Cartwright and Hansen, 2006; de Saint-Blanquat et al., 2006; Morgan et al., 2008; Galerne et al., 2011; Schofield et al., 2015; Magee et al., 2016; Wilson et al., 2016). For example, numerous studies have demonstrated that sill intrusions can: (1) locally heat and mature organic matter within the host rock, generating oil and/or gas (e.g., Rodriguez Monreal et al., 2009); (2) be associated with dome structures, which can be described as four-way dip closures (Hansen and Cartwright, 2006; Jackson et al., 2013; Magee et al., 2014; Magee et al., 2015); and (3) promote the development of local intense fracture networks that increase the permeability of the host rock (Witte et al., 2012; Agirrezabala, 2015; Senger et al., 2015). A robust understanding of the mechanics of magma emplacement in volcanic basins is therefore required in order to de-risk hydrocarbon exploration in volcanic basins (Potter and Konnerup-Madsen, 2003; Schutter, 2003a, b).

In this study, we focus on the mechanisms that control the growth of domes associated with igneous sills. These dome structures can represent structural traps, i.e., four-way dip

For Peer Review

closures, or create and deform stratigraphic traps, i.e., onlap of reservoir rocks and deflection of channels influencing the distribution of reservoir rocks for hydrocarbons. In recent years, distinct mechanisms controlling the formation of sill-associated doming have been proposed. The most common mechanism involves syn-emplacement uplift accommodating sill emplacement (e.g., Pollard and Johnson, 1973; Roman-Berdiel et al., 1995; Malthe-Sørenssen et al., 2004; Hansen and Cartwright, 2006; Kavanagh et al., 2006; Menand, 2008; Bunger and Cruden, 2011; Galerne et al., 2011; Galland, 2012; Galland et al., 2014; Galland et al., 2015). These models typically assume that uplift occurred via elastic bending, and sometime failure, of the overburden. However, field observations, seismic studies, and recent 3D laboratory models show that substantial syn-emplacement inelastic (elasto-plastic) deformation, such as local compaction and fluidization, can also affect the growth of the dome (e.g., Cosgrove and Hillier, 1999; Hansen and Cartwright, 2006; Schofield et al., 2010; Schofield et al., 2012a; Magee et al., 2013; Schofield et al., 2014). In addition to the syn-emplacement mechanisms, seismic data indicates that post-emplacement differential compaction may also play a role in the formation of dome structures above sills (e.g., Einsele et al., 1980; Cosgrove and Hillier, 1999; Hansen and Cartwright, 2006; Agirrezabala, 2015). However, the extent to which the interplay of syn-emplacement mechanisms vs. post-emplacement mechanisms control the final shape and structure of domes associated with igneous intrusions is currently not well known. This uncertainty typically emanates from the methods applied to study these systems. For example, structural field observations can provide small, detailed snapshots of intrusion overlying dome structures and associated fault and fracture systems, but they cannot not provide a complete spatial understanding due to incomplete outcropping conditions (e.g., Henry Mts; Wilson et al., 2016 and references therein). 2D seismic reflection profiles are also too incomplete to fully

For Peer Review

describe complex 3D structures (e.g., Planke et al., 2000; Berndt et al., 2001; Jackson et al., 2013; Zhao et al., 2014). Therefore, high-quality 3D seismic data is essential to study intrusion induced overburden deformation in 3D (Bell and Butcher, 2002; Smallwood and Maresh, 2002; Trude et al., 2003; Polteau et al., 2008; Magee et al., 2015; Planke et al., 2015).

In this paper, we show how the detailed analysis of high-quality seismic data can be used to test and constrain the relevance of mechanical models of dome growth accommodating the emplacement of igneous sills. We highlight the contribution of syn- and post-emplacement mechanisms of overburden deformation by using detailed mapped horizons from 3D seismic reflections, thickness maps and the application of various seismic attributes.

For Peer Review

MECHANISMS OF OVERBURDEN DEFORMATION

A range of different models derived from field observations and seismic imaging have been proposed to explain overburden deformation above sills, dominantly dome-shaped structures.

Syn-emplacement processes

Classic models of doming involve overburden uplift in response to elastic bending above an intruding sill or laccolith (Figure 1A) (Gilbert, 1877; Pollard and Johnson, 1973; Dixon and Simpson, 1987; Goulty and Schofield, 2008; Bunger and Cruden, 2011; Galland and Scheibert, 2013). In these models, doming occurs directly during the sill emplacement and the dome geometry is directly controlled by that of the underlying intrusion (e.g., Gilbert, 1877; Pollard and Johnson, 1973; Corry, 1988; Goulty and Schofield, 2008; Galland and Scheibert, 2013). The dome amplitude f therefore equals the sill thickness t (Figure 1A) (Pollard and Johnson, 1973;

Dixon and Simpson, 1987; Goulty and Schofield, 2008; Bunger and Cruden, 2011; Galland and Scheibert, 2013); both *f* and *t* can be used as a proxy for the volume of the dome and intrusion, respectively. This active doming is often referred to as forced-folding (e.g., du Toit, 1920; Stearns, 1978; Trude et al., 2003). Forced folding typically produces a positive topographic structure at the paleo-surface, such that sediments deposited contemporaneous to sill emplacement onlap onto the paleo-high (e.g., Trude et al., 2003; Schofield et al., 2015; Magee et al., 2016). The observation of these onlap features in seismic data provides a method of dating the intrusion emplacement (Trude et al., 2003).

For Peer Review

Elastic bending produces complex stress distributions in the overburden, resulting in outer-arc stretching and inner-arc compression (Timoshenko and Woinowsky-Krieger, 1959; Ramsay, 1967; Pollard and Johnson, 1973). This outer-arc stretching can lead to thinning of the uppermost layers of the dome (Ramsay, 1967). When the stresses generated in response to elastic bending exceed the strength of the overburden rocks, failure occurs and characteristic fracture patterns develop. These fracture pattern can be classified into four main types depending to their location in the overburden (Figure 1B): (1) circumferential, tensile fractures at the surface coincident with the area of the largest convex curvature above the sill edges (e.g., Pollard and Johnson, 1973; Bunger and Cruden, 2011; Galland et al., 2016); (2) radial tensile fractures (mode I) and/or normal faults (Mode II) due to an extensional regime (i.e. outer-arc stretching) in the central part of the dome structure (Hansen and Cartwright, 2006; Magee et al., 2013; Galland et al., 2016); (3) dilational fractures near the peripheral hinge of the dome close to the intrusion tips progressing towards the surface (Pollard and Johnson, 1973; Menand, 2008; Thomson and Schofield, 2008; Galland and Scheibert, 2013); and (4) shear fractures resulting from differential uplift at the dome edge (de Saint-Blanquat et al., 2006; Hansen and Cartwright, 2006; Agirrezabala, 2015; Wilson et al., 2016).

Although elastic bending promotes roof uplift, other mechanisms can affect the overall geometry of the dome structure above the intrusion. For example, pore fluid expulsion within the thermal and/or structural aureole of the intrusion can lead to a significant volume reduction of the host rock (Figure 1C) (Einsele et al., 1980; Morgan et al., 2008; Schofield et al., 2010; Schofield et al., 2012a; Jackson et al., 2013; Magee et al., 2013; Schofield et al., 2014). This volume reduction resulting from a decreased porosity reduces the effect of active mechanical doming due to the emplacement of the intrusion. Therefore the amplitude of the dome f is expected to be less than the sill thickness t (Figure 1C) implying that the host rock above the intrusion is thinner than outside the intrusion (Figure 1C).

Post-emplacement process

Variations in the load of post-emplacement sedimentation can induce a variable subsidence of the overburden due to differential compaction (Figure 1D) (e.g., Cosgrove and Hillier, 1999; Hansen and Cartwright, 2006). In particular, following the emplacement of the intrusion, the load due to post-emplacement sedimentation triggers compaction of the underlying rocks. Because the intrusions are virtually incompressible with respect to the surrounding sedimentary rocks, and therefore do not compact, a dome structure may develop (Figure 1D) (e.g., Cosgrove and Hillier, 1999; Agirrezabala, 2015). In addition to generating new folds, this differential compaction process can enhance the amplitude f of a pre-existing dome due to the emplacement of the intrusion, such that f becomes larger than the sill thickness t (Figure 1D).

For Peer Review

Another consequence is that the domed sequence is expected to be thicker above the sill than outside the sill (Figure 1D).

To summarize, these models are associated with distinct characteristic structures and features. To test the relevance of each model, we will test the occurrence, or not, of these structures and features in the Tulipan prospect case study, Møre Basin, mid-Norwegian continental margin.

GEOLOGICAL FRAMEWORK

Over the last three decades, massive sill complexes of at least 80000 km^2 have been imaged in the Møre and Vøring basins, offshore Norway by 2D and 3D seismic reflection data (e.g., Berndt et al., 2001; Planke et al., 2005). Positioned on the mid-Norwegian margin, the Møre Basin represents a type example of a rifted volcanic margin (Planke et al., 2005). The outline of the Møre Basin is defined by the base unconformity of the up to 6 km thick Cretaceous sedimentary basin infill (Figure 2A) (Brekke, 2000; Faleide et al., 2010). The development of the basin occurred during Late Jurassic – Early Cretaceous rifting of the Norwegian continental margin (Brekke, 2000 and references therein). Late Paleocene – Early Eocene rifting associated with the opening of the North Atlantic lead to the emplacement of a significant volume of igneous material within the sedimentary infill, which is composed of mainly claystone, with interbedded sandstone and sporadic carbonate intercalations (e.g., Dalland et al., 1988; Berndt et al., 2001; Planke et al., 2005).

The oldest stratigraphic unit in the area of interest is the Late Cretaceous Springar Formation, which consists mainly of claystone with carbonate intercalations. The uppermost

For Peer Review

sequence of the Springar Formation contains a prominent carbonate-cemented layer, which corresponds to the lowermost horizon interpreted in this study (Figure 3). The base of this carbonate layer, subsequently referred to as Base Carbonate, corresponds to a high positive reflection on the seismic data (Figures 3 & 5). Other horizons interpreted in this study include the Top Danian, HV4, HV3, and HV1, which are all contained in the Early Paleogene Tang Formation (Figure 3). The lower Tang Formation (Top Danian to Base Carbonate) is composed of a sandstone succession, which proved to be a reservoir rock in the Tulipan prospect, as highlighted by a gas discovery well (6302/6-1, abandoned) (Figure 2). The rest of the Tang Formation consists of dark gray claystone successions (Figure 3). The complete stratigraphic description of the Tulipan prospect can be found in Kjoberg et al. (this volume, submitted). The area of interest is located beyond the eastern limit of Paleogene basalts that cover the northwestern border of the Møre Basin (Figure 2) (e.g., Brekke, 2000; Berndt et al., 2001).

For Peer Review

DATA AND METHODS

This study uses a full-stack, time-migrated, zero-phase 3D seismic dataset (i.e. ST0105) that was processed in 2001 and covers the Tulipan prospect in the western part of the Møre Basin (Figure 2). The complete 3D survey covers an area of 1610 km^2, has a line spacing of 12.5 m, and was recorded to a depth of 7 s TWT. We focus on the northern c. 450 km^2 of the area containing the well 6302/6-1 (Figure 2). The 3D seismic data is displayed with a reverse polarity (i.e. a downward increase in acoustic impedance correlates to negative or blue reflections). In the time interval of interest (4.6-4.8 s TWT), the seismic data has an average frequency of 15-20 Hz. The range for the thickness of the sill was calculated using the dominant frequency in the area of the sill intrusion (15 Hz) and we used a value of velocity Vp = 5500 m/s (Planke et al., 2005;

Jackson et al., 2013) and the assumed error of about ±10% after Jackson et al. (2013). This suggests a thickness within the limit of separability ($\lambda/4$) of ~92 m (±10%) and the limit of detection ~12 m (±10%) for sills (Planke et al., 2005; Jackson et al., 2013).

Data from borehole 6302/6-1 was used to constrain the lithology, geophysical properties, and age of the strata in the interval of interest (Kjoberg et al., this volume, submitted). The well extends to a depth of 4234 m [m RKB], a total length of 15.7 m was cored between 3903 m and 3942 m in the Danian sandstone (Tang Formation) and cutting samples were taken in the interval of 1975-4230 m. Conventional borehole wireline logs and a check-shot (VSP) time-depth curve in combination with the core/cutting samples were used to develop a simple constant velocity model based on the interval velocities (Vp_{int}) to depth-convert the key horizons (Figure 3). These information combined with the 3D seismic data were used to interpret five key horizons (5 to 15 line interval inline/xline) in the sedimentary strata above the intrusion (Figure 3). 3D volume visualization (i.e. opacity rendering), and different surface and volume attributes (i.e. RMS-Amplitude, Coherence, spectral decomposition) were used to extract additional characteristics of the interpreted reflections in the sedimentary overburden of the Tulipan sill (Planke et al., 2015).

The interpretation of sills in the seismic data was performed according to their reflection properties, with laterally discontinuous, strata-discordant, high-amplitude anomalies considered to represent intrusions (Smallwood and Maresh, 2002; Polteau et al., 2008; Thomson and Schofield, 2008; Jackson et al., 2013; Magee et al., 2014; Planke et al., 2015). At the location of the Tulipan sill, constrained by Polteau et al. (2008), the seismic data display a high-amplitude reflection package (Figures 4 & 5). We define the top of the Tulipan sill as the uppermost trough of this reflection package (Figure 4 & 5). We interpreted the top of the sill with 2 line interval

For Peer Review

inline/xline resolution. The subsequent deeper peak reflection (Figure 4) was roughly picked (16 line interval inline/xline) as an estimate for the base of the Tulipan sill.

RESULTS

Structure of the sill

Figure 5 shows the 3D expression of the picked high-amplitude reflection of the top Tulipan sill, which consists of: (1) a flat, starta-concordant inner base with a c. 10-12 km diameter; and (2) flanking inclined outer sheets that transgress upwards and outwards (c. 200-400 ms TWT). The Tulipan sill thus displays a typical saucer-shaped geometry. The inclined sheets are laterally segmented radially, with the vertical offset between the segments increasing towards the outer rim (Figure 5).

The base of the Tulipan sill was not clearly observable in the tuned reflection package. The picked base shows lateral thickening of the reflection associated with a reduction in amplitude strength and the interruption of the continuous reflection, in the central part of the sill (Figure 4 & 5B). Because the sill is visible on the seismic data, the sill thickness is higher than the limit of detection, i.e. 12 m (±10%). However, since we cannot clearly separate the two reflections for the top and the bottom of the sill, the sill thickness is below the limit of separability of i.e. 92 m (±10%). This estimate is in agreement with other sill observations in the Møre and Vøring basins (e.g., Berndt et al., 2000).

Structure of the overburden

Time structure maps (TWT)

For Peer Review

In this study, five key horizons were interpreted in the sedimentary overburden (Figure 4). From top to bottom, these are: (1) HV1, describes the top of the deformed overburden locally downlapped by overlying reflections; (2) HV3, prominent reflection above lavas in the Tang Formation; (3) HV4, a stratigraphic surface that displays a prominent polygonal fault pattern; (4) Top Danian, which corresponds to the top of the sandstone unit representing the reservoir rock in the area; (5) Base Carbonate, a prominent Mesozoic carbonate layer (in the Late Springar Formation; Figures 3 & 4).

HV1 shows a central dome structure that correlates with the periphery of the underlying Tulipan sill (Figure 6A). The maximum amplitude f of this dome structure was calculated, i.e. using a best fitting plane for the estimation of the dome base, to be approximately $f \approx 50 \pm 20$ m (Figure 6B) from the depth converted time structure map. Figure 6A shows four additional dome structures surrounding the central dome: (1) one overprinting the outline of the central dome in the northwest, and (2) three separate ones in the south and east. A north-south trending depression separates these three domes from the large central dome above the Tulipan. The underlying time structure maps of the HV3, HV4, Top Danian and Base Carbonate horizons similarly display a large central dome as in HV1 (Figure 6C & supplemental material). Note that for the HV3, Top Danian and Base Carbonate, the data coverage is limited, such that the smaller peripheral domes are not imaged. Additionally, the time structure maps of the different horizons show that the well 6302/6-1 was drilled right in the crest of the dome above the Tulipan sill.

Spectral decomposition attribute maps on sedimentary horizons

For Peer Review

Spectral decomposition attribute maps were produced on the interpreted reflections in the sedimentary overburden of the sill to visualize possible host rock deformations (e.g. fractures, edges, etc., Figure 7).

The attribute map of the uppermost interpreted horizon, the HV1 shows 19 dark, circular features (white circles, Figure 7A), i.e. hydrothermal vent complexes that overlie the lateral termination of the underlying Tulipan sill. The majority of these vents are connected by thin, linear features. Similar circular and linear features were observed in the HV3 (yellow dashed line, Figure 7B) but they were to faint to be confidently described. A possible spatial correlation of those linear features between the different horizon maps cannot be evidenced with confidence (Figure 7A & B).

On the HV3 map (Figure 7B), dark circular features similar to those observed in HV4 (Figure 7C) also appear at the same locations as those observed in the HV4 map (black ovals, Figure 7B); note, however, that they are overall larger. Inside the Tulipan sill periphery, two separate areas can be distinguished: (1) a southern area (yellow dashed line, Figure 7B), which displays dark colors and a complex, but faint occurrence of circular features and linear features; and (2) a northern area characterized by bright colors with no observable features (Figure 7B). Outside the Tulipan sill periphery, two comprehensive dark areas in the northwest and northeast are visible (Figure 7B). We interpret these latter as the extruded Paleogene basalts (Berndt et al., 2001) according to their seismic character (Figure 2 & 3), the emplacement of which was not related to the emplacement of the Tulipan sill and associated doming. Therefore, we will not consider them in the following sections.

For Peer Review

The HV4 map highlights an overall coverage with linear features (Figure 7C), which correlate with discontinuities in the seismic reflection data (Figure 4). This polygonal pattern does not display a change in its characteristics inside or outside of the Tulipan periphery (Figure 7C). Other observable features are the dark circular patches with diameters up to c. 1 km (e.g., black circles, Figure 7C). They are mainly located along the edge of Tulipan sill, and correspond to vertical zones characterized by complex and weak seismic reflections cross-cutting the horizon (Figure 3). Such features are characteristic of hydrothermal vent complexes (e.g., Svensen et al., 2004; Planke et al., 2005).

The Top Danian horizon attribute map has a very limited spatial distribution inside the periphery of the Tulipan sill (Figure 3 and 7D). The central part of the horizon map is represented by an area of significantly bright colors, again highlighting lateral variations in rock properties (Figure 7D). No significant feature is visible.

The Base Carbonate horizon (Figure 7E) images the lowermost interpreted reflection in the sedimentary sequence above the Tulipan sill (Figure 3). The spectral decomposition map shows a distinct dark line-feature corresponding to the crossing of the Tulipan sill though the horizon (Figure 7E). No other prominent feature is visible. Within the Tulipan sill periphery and adjacent to it an overall bright color scheme is observed, highlighting lateral variations in rock properties.

Isochron maps

Isochron maps between different horizons were produced to quantify lateral thickness variations of the intervals through the dome above the Tulipan sill (Figure 3 & 8). This

For Peer Review

information is crucial for testing the different models listed in Figure 1. The 3D seismic data of the Tulipan prospect images a regional thickening of the sedimentary strata towards the west/northwest (Figure 8).

Figure 8A displays the isochron map of an interval (Top Tare – HV1) right above the assumed paleo-surface during the emplacement of the Tulipan sill (i.e. HV1). The interpretation of the Top Tare horizon used to produce this isochron map originates from the work of Kjoberg et al. (this volume, submitted). This interval shows distinct, thick circular mound structures that typically overlie the periphery of the underlying Tulipan sill at the same location as the hydrothermal vent complexes observed before (Figure 7A-C). The Top Tare – HV1 interval displays a thinning within the Tulipan periphery compared to the areas in the close vicinity of the underlying sill outline. Additionally, we observe fracture pattern between the mound structures and in the surrounding of the sill (Figure 8A) coinciding with the dark linear features observed in Figure 7A.

The HV1-Base Carbonate interval, i.e. the overall sequence analyzed in this study, shows relatively constant thickness, except localized thinner areas that parallel to the outline of the underlying sill (Figure 8B); these areas are likely related to hydrothermal vent complexes. However, each subinterval displays more complex patterns.

The shallower HV1-HV4 interval exhibits a local ring feature, aligned along the periphery of the underlying sill, which is thicker than the background thickness (Figure 8C). The spatial positions of these local thick areas correspond to the observed dark circular patches in the spectral decomposition attribute maps (Figure 7). These features are likely related to

For Peer Review

hydrothermal vent complexes (Kjoberg et al., this volume, submitted). The thickness of this interval is similar at the center of the underlying sill and outside the sill (Figure 8C).

In contrast to the HV1-HV4 interval, the deeper HV4-Base Carbonate interval exhibits a thickening constrained inside the outline of the Tulipan sill (Figure 8D). Note the prominent thin elongated features parallel to the periphery of the Tulipan sill. These features are not visible on the HV1-HV4 interval (Figure 8C), but they affect the whole studied interval, i.e. HV1-Base Carbonate (Figure 8B). Similarly to the HV4-Base Carbonate interval, the Top Danian-Base Carbonate subinterval also exhibits a thickening (supplementary material). The location of this thickening roughly correlates with that of the observed bright colors of the Top Danian spectral decomposition map (Figure 7D).

For Peer Review

INTERPRETATION

Sill structure and relation with dome

Our 3D reconstruction of the top Tulipan sill exhibits a characteristic saucer-shape, with a flat inner sill, which connects to transgressive inclined sheets that exhibit radial offsets (Figure 5). Such a structure is in good agreement with the two stage model of shallow magma emplacement, whereby an initial flat sill intrudes along a stratigraphic weakness, followed by an, upward, outward transgressive emplacement of inclined sheets (e.g., Malthe-Sørenssen et al., 2004; Hansen and Cartwright, 2006; Polteau et al., 2008; Thomson and Schofield, 2008; Galland, 2012). The radial offsets visible along the inclined sheets are interpreted as radial flow indicators, i.e. intrusive step and bridge structures indicating upward and outward magma flow during the emplacement into a brittle host rock (e.g., Thomson and Schofield, 2008; Hutton, 2009; Schofield et al., 2010; Magee et al., 2016 and the references therein), also in agreement with the two-stage model of saucer-shaped sill emplacement.

The Tulipan sill exhibits an overall spatial correlation with the overlying dome structure (Figure 6). The well data does not evidence any other sill emplaced in the sill overburden. The seismic data only displays a small, shallower sill in the western edge of the dome, resulting only in a local, shallow positive topographic feature (Figure 6; supplementary material). We thus conclude that the dome displayed in our data is solely related to the underlying Tulipan sill.

The HV1 horizon has been identified as being the paleo-surface at the time of emplacement of the Tulipan sill, based on the detailed interpretation of the hydrothermal vent complexes associated with the Tulipan sill (Kjoberg et al., this volume, submitted). This implies that the Tulipan sill emplaced between 55.8 and 54.9 Ma (Kjoberg et al., this volume, submitted), consistent with the age of the North Atlantic Large Igneous Province emplaced at the Paleocene–Eocene transition (Berndt et al., 2001; Svensen et al., 2004; Faleide et al., 2010). Thus, the depth of emplacement is estimated to be not deeper than 1.5-2 km. The saucer-shaped geometry of the Tulipan sill is a consequence of such a shallow emplacement depth (e.g., Planke et al., 2005; Galland et al., 2009; Eide et al., 2016).

Dome growth mechanisms

Our detailed analyses of the borehole and 3D seismic data allow us to test the relevance of the distinct mechanisms of dome growth above igneous sills. Our results highlight the occurrence of both post-emplacement and syn-emplacement processes.

Post-emplacement differential compaction

For Peer Review

The isochron maps of Figure 8B and D show that the HV1-Top Carbonate interval and the HV4-Carbonate subinterval are thicker above the Tulipan sill than outside the sill. This thickening is in good agreement with the differential compaction mechanism (Figure 1D). Thus, we conclude that differential compaction must have, at least partly, contributed to the formation of the dome structure above the Tulipan sill. A key question is thus whether parts of the dome have resulted from syn-emplacement mechanisms or not.

Syn-emplacement mechanisms

For Peer Review

The direct evidence of syn-emplacement mechanisms of dome growth above the Tulipan sill is limited. We observe fractures patterns located in the vicinity of, and parallel to, the Tulipan sill periphery and dome edge, affecting the paleo-surface horizon HV1 (Figure 7 & 8A). These surficial peripheral concentric tensile/extensional fractures are in good agreement with the laboratory experiments of dome growth of Galland (2012). These experiments show that when a dome associated with an intruding saucer-shaped sill exhibits a plateau shape, like that of the Tulipan dome, the largest convex curvature of the paleo-surface occurs near the upper, monoclonal hinges of the dome (see Figure 1). The resulting fractures are thus concentric, parallel, and close to the dome edge (see also Galland et al., 2016). The close relation between these tensile fractures and the hydrothermal vent complexes (Figures 7A & 8A) suggests that the former might have channeled the over-pressurized fluids, and so controlled partly the locations of the vents. Furthermore, the observed central thinning of the shallow interval (HV1-HV4) of the domed sedimentary sequence above the Tulipan sill (Figure 8C) are in good agreement with the observations of Ramsay (1967), who suggested that such thinning might result from outer-arc stretching of the apex of a growing forced fold. The presence of both concentric fractures and superficial thinning are the only evidence of forced-folding associated with the emplacement of the Tulipan sill might have happened.

Nevertheless, other indicators of syn-emplacement dome growth are not visible. The significant thickness variations of the sedimentary intervals affected by the doming do not support the solely application of the elastic bending model, which assumes constant thickness of the domed formations (e.g., Pollard and Johnson, 1973; Goulty and Schofield, 2008; Galland and Scheibert, 2013). In addition, we do not observe onlap structures on the domed morphology of the paleo-surface, which could confirm the short time scale of an intrusion-induced uplift of the overburden (Figure 1A) (e.g., Trude et al., 2003; Hansen and Cartwright, 2006; Magee et al., 2014). Finally, we do not observe tensile or extensional fractures at the apex of the dome, expected from brittle outer-arc stretching, as observed for instance by Magee et al. (2013). Nevertheless, we cannot rule out that such fractures, if present, are of sub-seismic scale and so invisible. In addition, the observed polygonal fault pattern observable in the whole area (Figure 7C), which formed 57.9 Ma ago prior to the emplacement of the sill Kjoberg et al., (this volume, submitted), do not show evidence of reactivation due to forced folding.

For Peer Review

In our results the range of the estimated thickness *t* of the Tulipan sill and the values of dome amplitude *f* show a significant overlap. However, due the uncertainties on the sill thickness, this dome amplitude/sill thickness ratio is not conclusive, such that it is not possible to confidently constrain the ratio of contribution of the possible mechanisms for overburden deformation, i.e. elastic bending, differential compaction, and aureole volume reduction.

Our data also highlights the occurrence of hydrothermal vents (Figure 6-8), which result from local fluidization within the host rock (Einsele et al., 1980; Svensen et al., 2004; Schofield et al., 2010; Schofield et al., 2012a; Jackson et al., 2013). Nevertheless, these authors show that fluidization occurs dominantly close to the intrusions, and the resulting structures are likely of sub-seismic scale and so invisible on our seismic data. In addition, the well within the study area is not deep enough to reach the sedimentary rocks near the Tulipan sill, therefore it is not useful to constrain the thickness of the fluidized rock formations (Figure 3 & 5B). Therefore, our data cannot allow us constraining to which extent fluidization has accommodated the sill emplacement, and so the dome growth dynamics.

For Peer Review

CONCLUSION

Our study utilizes analysis of 3D seismic and well data to test the occurrence of dome growth dynamics associated with the Tulipan sill. We highlight that a single mechanism cannot explain development of the dome, but rather we show that a combination of different mechanisms controlled the emplacement of the Tulipan sill and its associated deformation of the sedimentary overburden in the Tulipan prospect. The main findings of our study are listed below.

- The dome displayed in our data is solely related to the underlying Tulipan sill.
- Differential compaction must have, at least partly, contributed to the formation of the dome structure above the Tulipan sill.
- Elastic bending had only a minor contribution to the accommodated deformation in the overburden of the Tulipan sill.
- We infer the formation of dilational fractures in the vicinity and parallel to the Tulipan periphery connecting hydrothermal vents. However, we cannot exclude the fact, that some of the features might be: (1) circumferential tensile fractures at

the surface or (2) shear fractures resulting from differential uplift at the dome edge.

- We cannot confidently observe the process of outer-arc stretching, due to missing observations of associated fracture systems in the crest of the domed overburden.
- Polygonal faults formed prior to the emplacement of the sill do not show evidence of reactivation due to the doming.

Future studies should concentrate on the quantitative influence of compaction on the amplitude of the domed overburden in relation to the underlying intrusion thickness. Therefore, 3D seismic data from directly drilled sills and the associated overburden would contribute to essentially to better constrain the accommodated deformation induced by an intrusion.

ACKNOWLEDGMENTS

We thank Statoil for providing us with the PL251 (Tulipan) geophysical and geological reports for well 6302/6-1. Thanks to GeoTerric and Schlumberger (Petrel) for the free academic use of seismic software. We further acknowledge the support from the Research Council of Norway through its Centers of Excellence funding scheme, project 223272, and from the MIMES project.

APPENDICES

-

REFERENCES

For Peer Review

Agirrezabala, L. M., 2015, Syndepositional forced folding and related fluid plumbing above a magmatic laccolith: Insights from outcrop (Lower Cretaceous, Basque-Cantabrian Basin, western Pyrenees): Geological Society of America Bulletin, 982-1000, doi: 10.1130/b31192.1.

Bell, B., and Butcher, H., 2002, On the emplacement of sill complexes: evidence from the Faroe-Shetland Basin: Geological Society, London, Special Publications: **197**, no. 1, 307-329, doi: 10.1144/gsl.sp.2002.197.01.12.

Berndt, C., Planke, S., Alvestad, E., Tsikalas, F., and Rasmussen, T., 2001, Seismic volcanostratigraphy of the Norwegian Margin: constraints on tectonomagmatic break-up processes: Journal of the Geological Society: **158**, no. 3, 413-426, doi: 10.1144/jgs.158.3.413.

Berndt, C., Skogly, O. P., Planke, S., Eldholm, O., and Mjelde, R., 2000, High-velocity breakup-related sills in the Vøring Basin, off Norway: Journal of Geophysical Research: Solid Earth: **105**, no. B12, 28443-28454, doi: 10.1029/2000JB900217.

Brekke, H., 2000, The tectonic evolution of the Norwegian Sea Continental Margin with emphasis on the Vøring and Møre Basins: Geological Society, London, Special Publications: **167**, no. 1, 327-378, doi: 10.1144/gsl.sp.2000.167.01.13.

Bunger, A. P., and Cruden, A. R., 2011, Modeling the growth of laccoliths and large mafic sills: Role of magma body forces: Journal of Geophysical Research: Solid Earth: **116**, no. B2, doi: 10.1029/2010JB007648.

Cartwright, J., and Hansen, D. M., 2006, Magma transport through the crust via interconnected sill complexes: Geology: **34**, no. 11, 929-932, doi: 10.1130/g22758a.1.

Corry, C. E., 1988, Laccoliths: mechanics of emplacement and growth, Geological Society of America Special Paper, v. 220, 110 p.

For Peer Review

Cosgrove, J. W., and Hillier, R. D., 1999, Forced-fold development within Tertiary sediments of the Alba Field, UKCS: evidence of differential compaction and post-depositional sandstone remobilization: Geological Society, London, Special Publications: **169**, no. 1, 61-71, doi: 10.1144/gsl.sp.2000.169.01.05.

Dalland, A., Worsley, D., and Ofstad, K., 1988, A lithostratigraphic scheme for the mesozoic and cenozoic and succession offshore mid-and northern norway, Oljedirektoratet.

de Saint-Blanquat, M., Habert, G., Horsman, E., Morgan, S. S., Tikoff, B., Launeau, P., and Gleizes, G., 2006, Mechanisms and duration of non-tectonically assisted magma emplacement in the upper crust: The Black Mesa pluton, Henry Mountains, Utah: Tectonophysics: **428**, no. 1–4, 1-31, doi: 10.1016/j.tecto.2006.07.014.

Dixon, J. M., and Simpson, D. G., 1987, Centrifuge modelling of laccolith intrusion: Journal of Structural Geology: **9**, no. 1, 87-103, doi: 10.1016/0191-8141(87)90046-0.

du Toit, A., 1920, The Karoo dolerites of South Africa: a study in hypabyssal injection: Transactions of the Geological Society of South Africa: **23**, 1-42,

Eide, C. H., Schofield, N., Jerram, D. A., and Howell, J. A., 2016, Basin-scale architecture of deeply emplaced sill complexes: Jameson Land, East Greenland: Journal of the Geological Society, 10.1144/jgs2016-018.

Einsele, G., Gieskes, J. M., Curray, J., Moore, D. M., Aguayo, E., Aubry, M.-P., Fornari, D., Guerrero, J., Kastner, M., Kelts, K., Lyle, M., Matoba, Y., Molina-Cruz, A., Niemitz, J., Rueda, J., Saunders, A., Schrader, H., Simoneit, B., and Vacquier, V., 1980, Intrusion of basaltic sills into highly porous sediments, and resulting hydrothermal activity: Nature: **283**, no. 5746, 441-445, doi: 10.1038/283441a0.

For Peer Review

Faleide, J. I., Bjørlykke, K., and Gabrielsen, R. H., 2010, Geology of the Norwegian Continental Shelf, Petroleum Geoscience, Springer, 467-499, doi: 10.1007/978-3-642-34132-8_25.

Galerne, C. Y., Galland, O., Neumann, E.-R., and Planke, S., 2011, 3D relationships between sills and their feeders: evidence from the Golden Valley Sill Complex (Karoo Basin) and experimental modelling: Journal of Volcanology and Geothermal Research: **202**, no. 3–4, 189-199, doi: 10.1016/j.jvolgeores.2011.02.006.

Galland, O., 2012, Experimental modelling of ground deformation associated with shallow magma intrusions: Earth and Planetary Science Letters: **317–318**, no. 0, 145-156, doi: 10.1016/j.epsl.2011.10.017.

Galland, O., Bertelsen, H. S., Guldstrand, F., Girod, L., Johannessen, R. F., Bjugger, F., Burchardt, S., and Mair, K., 2016, Application of open-source photogrammetric software MicMac for monitoring surface deformation in laboratory models: Journal of Geophysical Research: Solid Earth, 21, doi: 10.1002/2015JB012564.

Galland, O., Burchardt, S., Hallot, E., Mourgues, R., and Bulois, C., 2014, Dynamics of dikes versus cone sheets in volcanic systems: Journal of Geophysical Research: Solid Earth: **119**, no. 8, 6178-6192, doi: 10.1002/2014JB011059.

Galland, O., Holohan, E., van Wyk de Vries, B., and Burchardt, S., 2015, Laboratory Modelling of Volcano Plumbing Systems: A Review, Springer Berlin Heidelberg, 1-68, doi: 10.1007/11157_2015_9.

Galland, O., Planke, S., Neumann, E.-R., and Malthe-Sørenssen, A., 2009, Experimental modelling of shallow magma emplacement: Application to saucer-shaped intrusions: Earth and Planetary Science Letters: **277**, no. 3–4, 373-383, doi: 10.1016/j.epsl.2008.11.003.

For Peer Review

Galland, O., and Scheibert, J., 2013, Analytical model of surface uplift above axisymmetric flat-lying magma intrusions: Implications for sill emplacement and geodesy: Journal of Volcanology and Geothermal Research: **253**, 114-130, doi: 10.1016/j.jvolgeores.2012.12.006.

Gilbert, G. K., 1877, Report on the Geology of the Henry Mountains, Washington, U. S. Geographical Geological Survey of the Rocky Mountain, Region.

Goulty, N. R., and Schofield, N., 2008, Implications of simple flexure theory for the formation of saucer-shaped sills: Journal of Structural Geology: **30**, no. 7, 812-817, doi: 10.1016/j.jsg.2008.04.002.

Hansen, D. M., and Cartwright, J., 2006, The three-dimensional geometry and growth of forced folds above saucer-shaped igneous sills: Journal of Structural Geology: **28**, no. 8, 1520-1535, doi: 10.1016/j.jsg.2006.04.004.

Hutton, D., 2009, Insights into magmatism in volcanic margins: bridge structures and a new mechanism of basic sill emplacement–Theron Mountains, Antarctica: Petroleum Geoscience: **15**, no. 3, 269-278, doi: 10.1144/1354-079309-841.

Jackson, C. A.-L., Schofield, N., and Golenkov, B., 2013, Geometry and controls on the development of igneous sill–related forced folds: A 2-D seismic reflection case study from offshore southern Australia: Geological Society of America Bulletin: **125**, no. 11-12, 1874-1890, doi: 10.1130/b30833.1.

Kavanagh, J. L., Menand, T., and Sparks, R. S. J., 2006, An experimental investigation of sill formation and propagation in layered elastic media: Earth and Planetary Science Letters: **245**, no. 3–4, 799-813, doi: 10.1016/j.epsl.2006.03.025.

For Peer Review

Kay, S. M., Mancilla, O., and Copeland, P., 2006, Evolution of the late Miocene Chachahuén volcanic complex at 37°S over a transient shallow subduction zone under the Neuquén Andes: Geological Society of America Special Papers: **407**, 215-246, 10.1130/2006.2407(10).

Kontorovich, A. E., Khomenko, A. V., Burshtein, L. M., Likhanov, I. I., Pavlov, A. L., Staroseltsev, V. S., and Ten, A. A., 1997, Intense basic magmatism in the Tunguska petroleum basin, eastern Siberia, Russia: Petroleum Geoscience: **3**, no. 4, 359-369, 10.1144/petgeo.3.4.359.

Magee, C., Briggs, F., and Jackson, C. A. L., 2013, Lithological controls on igneous intrusion-induced ground deformation: Journal of the Geological Society: **170**, no. 6, 853-856, doi: 10.1144/jgs2013-029.

Magee, C., Jackson, C. A.-L., and Schofield, N., 2014, Diachronous sub-volcanic intrusion along deep-water margins: insights from the Irish Rockall Basin: Basin Research: **26**, no. 1, 85-105, doi: 10.1111/bre.12044.

Magee, C., Maharaj, S. M., Wrona, T., and Jackson, C. A.-L., 2015, Controls on the expression of igneous intrusions in seismic reflection data: Geosphere: **11**, no. 4, 1024-1041, doi: 10.1130/ges01150.1.

Magee, C., Muirhead, J. D., Karvelas, A., Holford, S. P., Jackson, C. A. L., Bastow, I. D., Schofield, N., Stevenson, C. T. E., McLean, C., and McCarthy, W., 2016, Lateral magma flow in mafic sill complexes: Geosphere, 33,

Malthe-Sørenssen, A., Planke, S., Svensen, H., and Jamtveit, B., 2004, Formation of saucer-shaped sills: Geological Society, London, Special Publications: **234**, no. 1, 215-227, doi: 10.1144/gsl.sp.2004.234.01.13.

For Peer Review

Menand, T., 2008, The mechanics and dynamics of sills in layered elastic rocks and their implications for the growth of laccoliths and other igneous complexes: Earth and Planetary Science Letters: **267**, no. 1–2, 93-99, doi: 10.1016/j.epsl.2007.11.043.

Morgan, S., Stanik, A., Horsman, E., Tikoff, B., de Saint Blanquat, M., and Habert, G., 2008, Emplacement of multiple magma sheets and wall rock deformation: Trachyte Mesa intrusion, Henry Mountains, Utah: Journal of Structural Geology: **30**, no. 4, 491-512, doi: 10.1016/j.jsg.2008.01.005.

Planke, S., Rasmussen, T., Rey, S. S., and Myklebust, R., 2005, Seismic characteristics and distribution of volcanic intrusions and hydrothermal vent complexes in the Vøring and Møre basins: Geological Society, London, Petroleum Geology Conference series: **6**, 833-844, doi: 10.1144/0060833.

Planke, S., Svensen, H., Myklebust, R., Bannister, S., Manton, B., and Lorenz, L., 2015, Geophysics and Remote Sensing: Berlin, Heidelberg, Springer Berlin Heidelberg, 1-16, doi: 10.1007/11157_2014_6.

Planke, S., Symonds, P. A., Alvestad, E., and Skogseid, J., 2000, Seismic volcanostratigraphy of large-volume basaltic extrusive complexes on rifted margins: Journal of Geophysical Research: Solid Earth: **105**, no. B8, 19335-19351, doi: 10.1029/1999JB900005.

Pollard, D. D., and Johnson, A. M., 1973, Mechanics of growth of some laccolithic intrusions in the Henry mountains, Utah, II: Bending and failure of overburden layers and sill formation: Tectonophysics: **18**, no. 3–4, 311-354, doi: 10.1016/0040-1951(73)90051-6.

Polteau, S., Mazzini, A., Galland, O., Planke, S., and Malthe-Sørenssen, A., 2008, Saucer-shaped intrusions: Occurrences, emplacement and implications: Earth and Planetary Science Letters: **266**, no. 1–2, 195-204, doi: 10.1016/j.epsl.2007.11.015.

For Peer Review

Potter, J., and Konnerup-Madsen, J., 2003, A review of the occurrence and origin of abiogenic hydrocarbons in igneous rocks: Hydrocarbons in Crystalline Rocks: **214**, no. 1, 151-173, doi 10.1144/Gsl.Sp.2003.214.01.10.

Ramsay, J. G., 1967, Folding and fracturing of rocks, McGraw-Hill Companies.

Rodriguez Monreal, F., Villar, H. J., Baudino, R., Delpino, D., and Zencich, S., 2009, Modeling an atypical petroleum system: A case study of hydrocarbon generation, migration and accumulation related to igneous intrusions in the Neuquen Basin, Argentina: Marine and Petroleum Geology: **26**, no. 4, 590-605, doi: 10.1016/j.marpetgeo.2009.01.005.

Roman-Berdiel, T., Gapais, D., and Brun, J. P., 1995, Analogue models of laccolith formation: Journal of Structural Geology: **17**, no. 9, 1337-1346, doi: 10.1016/0191-8141(95)00012-3.

Schofield, N., Alsop, I., Warren, J., Underhill, J. R., Lehné, R., Beer, W., and Lukas, V., 2014, Mobilizing salt: Magma-salt interactions: Geology: **42**, no. 7, 599-602, 10.1130/g35406.1.

Schofield, N., Brown, D. J., Magee, C., and Stevenson, C. T., 2012a, Sill morphology and comparison of brittle and non-brittle emplacement mechanisms: Journal of the Geological Society: **169**, no. 2, 127-141, doi: 10.1144/0016-76492011-078.

Schofield, N., Heaton, L., Holford, S. P., Archer, S. G., Jackson, C. A.-L., and Jolley, D. W., 2012b, Seismic imaging of ‘broken bridges’: linking seismic to outcrop-scale investigations of intrusive magma lobes: Journal of the Geological Society: **169**, no. 4, 421-426, 10.1144/0016-76492011-150.

Schofield, N., Holford, S., Millett, J., Brown, D., Jolley, D., Passey, S. R., Muirhead, D., Grove, C., Magee, C., Murray, J., Hole, M., Jackson, C. A.-L., and Stevenson, C., 2015, Regional magma plumbing and emplacement mechanisms of the Faroe-Shetland Sill Complex:

For Peer Review

implications for magma transport and petroleum systems within sedimentary basins: Basin Research, 1-23, doi: 10.1111/bre.12164.

Schofield, N., Stevenson, C., and Reston, T., 2010, Magma fingers and host rock fluidization in the emplacement of sills: Geology: **38**, no. 1, 63-66, 10.1130/g30142.1.

Schutter, S. R., 2003a, Hydrocarbon occurrence and exploration in and around igneous rocks: Hydrocarbons in Crystalline Rocks: **214**, no. 1, 7-33, doi 10.1144/Gsl.Sp.2003.214.01.02.

Schutter, S. R., 2003b, Occurrences of hydrocarbons in and around igneous rocks: Hydrocarbons in Crystalline Rocks: **214**, no. 1, 35-68, doi 10.1144/Gsl.Sp.2003.214.01.03.

Senger, K., Buckley, S. J., Chevallier, L., Fagereng, Å., Galland, O., Kurz, T. H., Ogata, K., Planke, S., and Tveranger, J., 2015, Fracturing of doleritic intrusions and associated contact zones: Implications for fluid flow in volcanic basins: Journal of African Earth Sciences: **102**, no. 0, 70-85, doi: 10.1016/j.jafrearsci.2014.10.019.

Smallwood, J. R., and Maresh, J., 2002, The properties, morphology and distribution of igneous sills: modelling, borehole data and 3D seismic from the Faroe-Shetland area: Geological Society, London, Special Publications: **197**, no. 1, 271-306, doi: 10.1144/gsl.sp.2002.197.01.11.

Stearns, D. W., 1978, Faulting and forced folding in the Rocky Mountains foreland: Geological Society of America Memoirs: **151**, 1-38, doi: 10.1130/MEM151-p1.

Svensen, H., Corfu, F., Polteau, S., Hammer, Ø., and Planke, S., 2012, Rapid magma emplacement in the Karoo Large Igneous Province: Earth and Planetary Science Letters: **325–326**, 1-9, doi: 10.1016/j.epsl.2012.01.015.

Svensen, H., Planke, S., Malthe-Sørenssen, A., Jamtveit, B., Myklebust, R., Rasmussen Eidem, T., and Rey, S. S., 2004, Release of methane from a volcanic basin as a mechanism for initial Eocene global warming: Nature: **429**, no. 6991, 542-545, doi: 10.1038/nature02566.

For Peer Review

Thomson, K., and Hutton, D., 2004, Geometry and growth of sill complexes: insights using 3D seismic from the North Rockall Trough: Bulletin of Volcanology: **66**, no. 4, 364-375, doi: 10.1007/s00445-003-0320-z.

Thomson, K., and Schofield, N., 2008, Lithological and structural controls on the emplacement and morphology of sills in sedimentary basins: Geological Society, London, Special Publications: **302**, no. 1, 31-44, doi: 10.1144/SP302.3.

Timoshenko, S. P., and Woinowsky-Krieger, S., 1959, Theory of plates and shells, McGraw-hill Book Company.

Trude, J., Cartwright, J., Davies, R. J., and Smallwood, J. R., 2003, New technique for dating igneous sills: Geology: **31**, no. 9, 813-816, doi: 10.1130/g19559.1.

Wilson, P. I. R., McCaffrey, K. J. W., Wilson, R. W., Jarvis, I., and Holdsworth, R. E., 2016, Deformation structures associated with the Trachyte Mesa intrusion, Henry Mountains, Utah: Implications for sill and laccolith emplacement mechanisms: Journal of Structural Geology: **87**, 30-46, doi: 10.1016/j.jsg.2016.04.001.

Witte, J., Bonora, M., Carbone, C., and Oncken, O., 2012, Fracture evolution in oil-producing sills of the Rio Grande Valley, northern Neuquen Basin, Argentina: AAPG Bulletin: **96**, no. 7, 1253-1277, doi: 10.1306/10181110152.

Zhao, F., Wu, S., Sun, Q., Huuse, M., Li, W., and Wang, Z., 2014, Submarine volcanic mounds in the Pearl River Mouth Basin, northern South China Sea: Marine Geology: **355**, 162-172, doi: 10.1016/j.margeo.2014.05.018.

For Peer Review

LIST OF FIGURES

Figure 1: Schematic diagrams showing mechanisms of overburden deformation associated with intrusion emplacement. (A) Simple elastic model envisages the formation of a dome structure (forced fold) above an intrusion (e.g., Pollard and Johnson, 1973; Galland and Scheibert, 2013). (B) Four fracture types related to elastic overburden deformation: (1) circumferential, tensile fractures coincident with the area of the largest convex curvature of the dome (e.g., Pollard and Johnson, 1973; Bunger and Cruden, 2011; Galland et al., 2016); (2) radial tensile fractures (Mode I) and/or normal faults (Mode II) due to outer-arc stretching (Hansen and Cartwright, 2006; Magee et al., 2013; Galland et al., 2016); (3) dilational fractures progressing towards the surface (Pollard and Johnson, 1973; Menand, 2008; Thomson and Schofield, 2008; Galland and Scheibert, 2013); and (4) shear fractures resulting from differential uplift (de Saint-Blanquat et al., 2006; Hansen and Cartwright, 2006; Agirrezabala, 2015; Wilson et al., 2016). (C) Model of volume reduction, i.e. porosity decrease, affected by the aureole of the intrusion (e.g., Hansen and Cartwright, 2006; Jackson et al., 2013). (D) Differential compaction model envisages the formation and/or enhancement of a dome structure associated with an intrusion under the load of post-emplacement sedimentation (e.g., Cosgrove and Hillier, 1999; Hansen and Cartwright, 2006).

Figure 2: Location maps. (A) Position of the 3D seismic survey containing the Tulipan prospect in the Møre Basin on the Norwegian continental shelf with respect to the Norwegian mainland. Outline of the Paleogene basalts after (Berndt et al., 2001). (B) Seismic reflection time-slice showing the main igneous complexes identified in the study area. The Tulipan sill is indicated (*dashed line*) in addition to the location of well 6302/6-1.

For Peer Review

Figure 3: Simplified stratigraphic column of the study area showing the principal lithology encountered in the well. The period (*Pd*), epoch (*Ep*), group (*Gp*), and formation (*Fm*) are based on the biostratigraphy from cutting samples of well 6302/6-1 (e.g., Kjoberg et al., this volume, submitted). Interval velocities (Vp_{int}) used in the study derived from the VSP checkshot data. The lithological column (*Litho*) is based on and described in detail in Kjoberg et al., (this volume, submitted). The lithology below the total depth (*TD*) of the well is an extrapolation. Overview for the interpreted horizons (*Horizons*) used in this study.

Figure 4: Seismic stratigraphic framework, including a description of the mapped seismic reflections and the seismic sequences they define.

Figure 5: Seismic expression of the Tulipan sill. (A) 3D visualization of the saucer-shaped geometry of the top Tulipan sill horizon. Radial magma flow indicators mark edges of reflection segments representing upward, outward transgressing, igneous inclined sheets (Schofield et al., 2012b; Magee et al., 2014). (B) Seismic profiles show the cross-sectional expressions of the Tulipan sill (see (A) for location). P1 – P1' highlights the picked Tulipan sill top and base, whereas P2 – P2' visualizes the segmented character of the Tulipan sill reflection and indicates an underlying sill (*S*) below the Tulipan sill (Tulipan top - *white dashed line; black dashed line* tentatively interpreted as the sill base).

Figure 6: Time structure maps (two way travel time, TWT) and dome amplitude *f*. (A) HV1 time structure map shows the paleo-surface and top of the domed overburden during the emplacement of the Tulipan sill. (B) The stack of altitude data points within the Tulipan periphery highlights the plateau in the domed overburden. A best fit plane was used to estimate the base of the dome and calculate the amplitude *f* (*red area*). (C) Base Carbonate time structure

For Peer Review

map of the lowermost interpreted horizon above the Tulipan sill shows a good confined dome structure inside the Tulipan sill periphery. Subset shows the stratigraphic location of the (A) and (C).

Figure 7: Spectral decomposition attributes maps of key horizons. Subsets display the same seismic section of Figure 3 (for location see Figure 2). The periphery of the Tulipan sill (*red dashed line*) corresponds to the map contour at the level of c. 4400 ms (TWT). (A) HV1 (Top Tang Formation) defines the top of the dome structure, and highlights hydrothermal vent complexes (HTVCs, *white circles*) and fractures in between (*black/white arrows*). (B) HTVCs on HV3 are obscured by lava flow pattern (*outside the white lines*). (C) HV4 envisages a regional polygonal fault system, and deeper parts of the HTVCs (*black circles*) identified in (A). (D) Top Danian shows no fractures in the top of the reservoir sandstones of the Tulipan prospect. (E) The Base Carbonate shows no evidence for central fractures, but highlights the crosscut of the underlying Tulipan sill. (The crosscut itself is not visible in the seismic subset).

Figure 8: Thickness maps of the sedimentary sequences above the Tulipan sill. (A) Top Tare – HV1 isochron map shows the thickness anomalies (i.e. hydrothermal vent complex related mounds) in sedimentary strata right above the dome structure. (B) Isochron map of the complete strata interpreted (HV1 – Base Carbonate). *White line* shows the position of the seismic subset. (C) The upper dome structure, i.e. HV1 – HV4 isochron map, shows patchy thickness anomalies (thicker) in the close vicinity of the Tulipan sill periphery, whereas the central area is thin. (D) Isochron map of HV4 to Base Carbonate displays a contrasting thickness variation compared to (C) within the Tulipan sill periphery.

For Peer Review

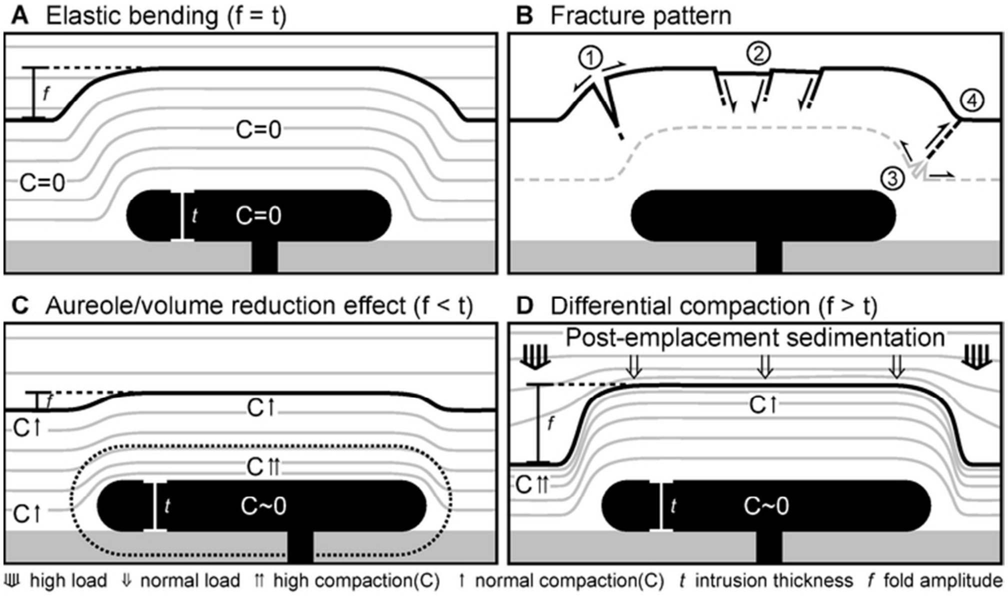

Figure 1: Schematic diagrams showing mechanisms of overburden deformation associated with intrusion emplacement. (A) Simple elastic model envisages the formation of a dome structure (forced fold) above an intrusion (e.g., Pollard and Johnson, 1973; Galland and Scheibert, 2013). (B) Four fracture types related to elastic overburden deformation: (1) circumferential, tensile fractures coincident with the area of the largest convex curvature of the dome (e.g., Pollard and Johnson, 1973; Bunger and Cruden, 2011; Galland et al., 2016); (2) radial tensile fractures (Mode I) and/or normal faults (Mode II) due to outer-arc stretching (Hansen and Cartwright, 2006; Magee et al., 2013; Galland et al., 2016); (3) dilational fractures progressing towards the surface (Pollard and Johnson, 1973; Menand, 2008; Thomson and Schofield, 2008; Galland and Scheibert, 2013; Agirrezabala, 2015); and (4) shear fractures resulting from differential uplift (de Saint-Blanquat et al., 2006; Hansen and Cartwright, 2006; Wilson et al., 2016). (C) Model of volume reduction, i.e. porosity decrease, affected by the aureole of the intrusion (e.g., Hansen and Cartwright, 2006; Jackson et al., 2013). (D) Differential compaction model envisages the formation and/or enhancement of a dome structure associated with an intrusion under the load of post-emplacement sedimentation (e.g., Cosgrove and Hillier, 1999; Hansen and Cartwright, 2006).

Figure 1

65x38mm (300 x 300 DPI)

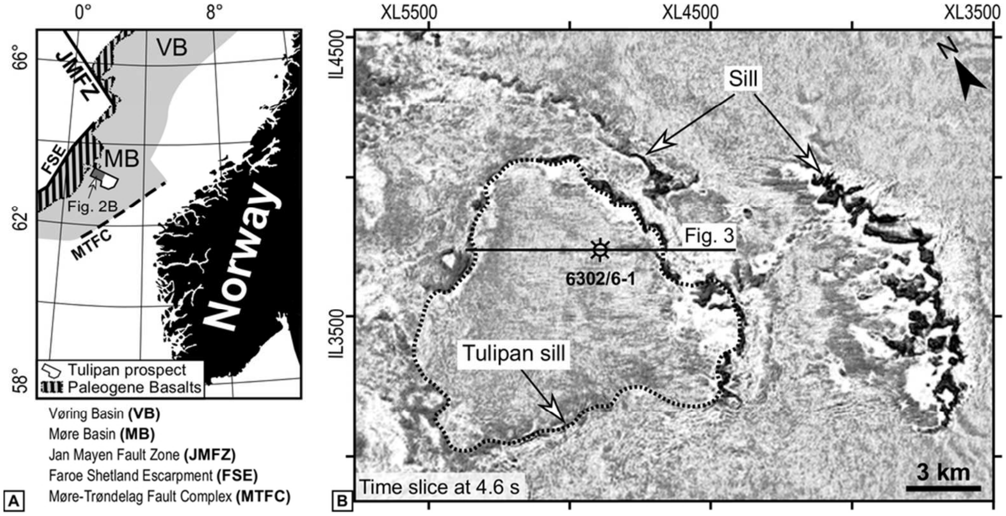

Figure 2: Location maps. (A) Position of the 3D seismic survey containing the Tulipan prospect in the Møre Basin on the Norwegian continental shelf with respect to the Norwegian mainland. Outline of the Paleogene basalts after (Berndt et al., 2001). (B) Seismic reflection time-slice showing the main igneous complexes identified in the study area. The Tulipan sill is indicated (dashed line) in addition to the location of well 6302/6-1.

Figure 2

89x45mm (300 x 300 DPI)

Review

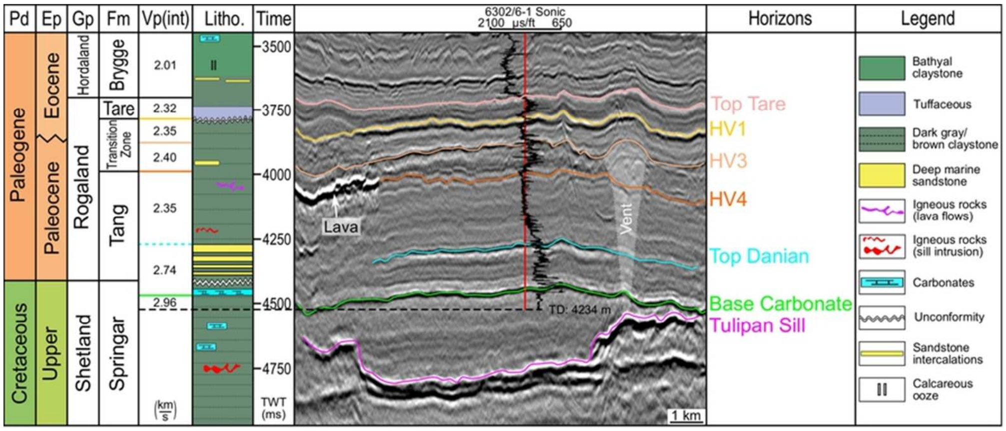

Figure 3: Simplified stratigraphic column of the study area showing the principal lithology encountered in the well. The period (Pd), epoch (Ep), group (Gp), and formation (Fm) are based on the biostratigraphy from cutting samples of well 6302/6-1 (e.g., Kjoberg et al., this volume, submitted). Interval velocities (Vpint) used in the study derived from the VSP checkshot data. The lithological column (Litho) is based on and described in detail in Kjoberg et al., (this volume, submitted). The lithology below the total depth (TD) of the well is an extrapolation. Overview for the interpreted horizons (Horizons) used in this study.
Figure 3
75x32mm (300 x 300 DPI)

er Review

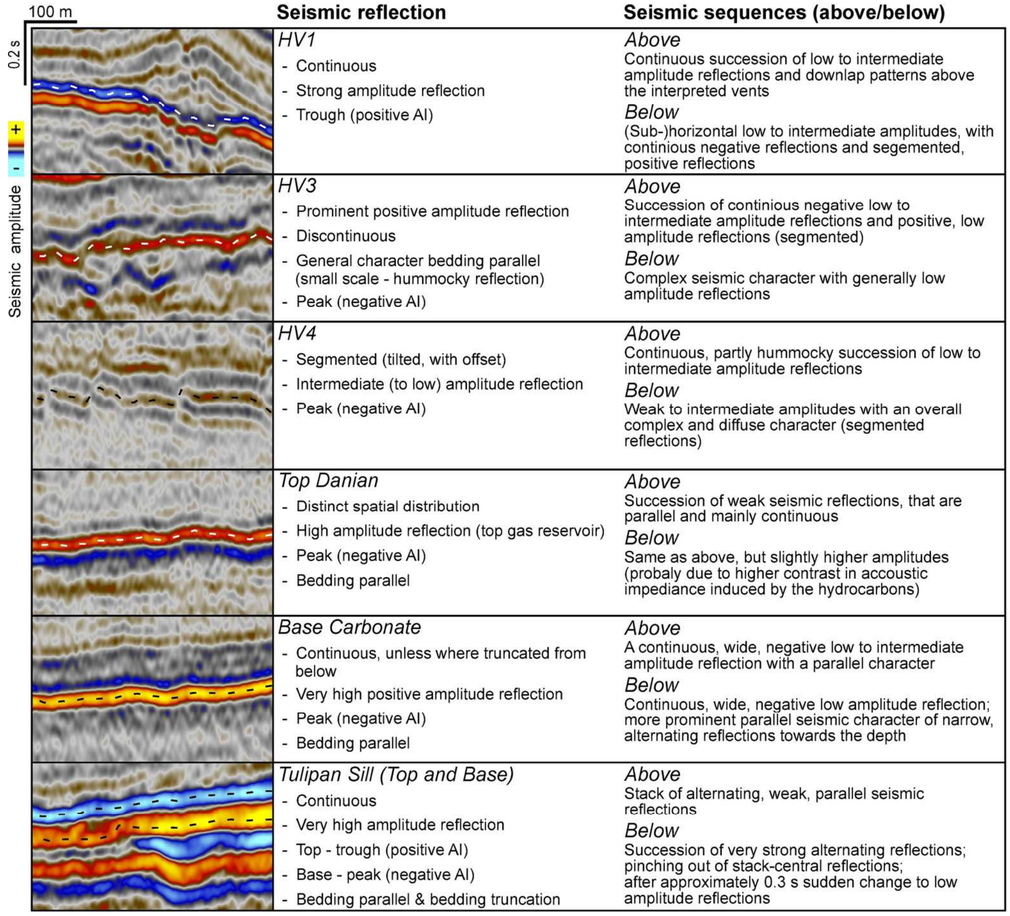

Seismic reflection	Seismic sequences (above/below)
HV1 - Continuous - Strong amplitude reflection - Trough (positive AI)	*Above* Continuous succession of low to intermediate amplitude reflections and downlap patterns above the interpreted vents *Below* (Sub-)horizontal low to intermediate amplitudes, with continious negative reflections and segemented, positive reflections
HV3 - Prominent positive amplitude reflection - Discontinuous - General character bedding parallel (small scale - hummocky reflection) - Peak (negative AI)	*Above* Succession of continious negative low to intermediate amplitude reflections and positive, low amplitude reflections (segmented) *Below* Complex seismic character with generally low amplitude reflections
HV4 - Segmented (tilted, with offset) - Intermediate (to low) amplitude reflection - Peak (negative AI)	*Above* Continuous, partly hummocky succession of low to intermediate amplitude reflections *Below* Weak to intermediate amplitudes with an overall complex and diffuse character (segmented reflections)
Top Danian - Distinct spatial distribution - High amplitude reflection (top gas reservoir) - Peak (negative AI) - Bedding parallel	*Above* Succession of weak seismic reflections, that are parallel and mainly continuous *Below* Same as above, but slightly higher amplitudes (probaly due to higher contrast in accoustic impediance induced by the hydrocarbons)
Base Carbonate - Continuous, unless where truncated from below - Very high positive amplitude reflection - Peak (negative AI) - Bedding parallel	*Above* A continuous, wide, negative low to intermediate amplitude reflection with a parallel character *Below* Continuous, wide, negative low amplitude reflection; more prominent parallel seismic character of narrow, alternating reflections towards the depth
Tulipan Sill (Top and Base) - Continuous - Very high amplitude reflection - Top - trough (positive AI) - Base - peak (negative AI) - Bedding parallel & bedding truncation	*Above* Stack of alternating, weak, parallel seismic reflections *Below* Succession of very strong alternating reflections; pinching out of stack-central reflections; after approximately 0.3 s sudden change to low amplitude reflections

Figure 4: Seismic stratigraphic framework, including a description of the mapped seismic reflections and the seismic sequences they define.
Figure 4
161x147mm (300 x 300 DPI)

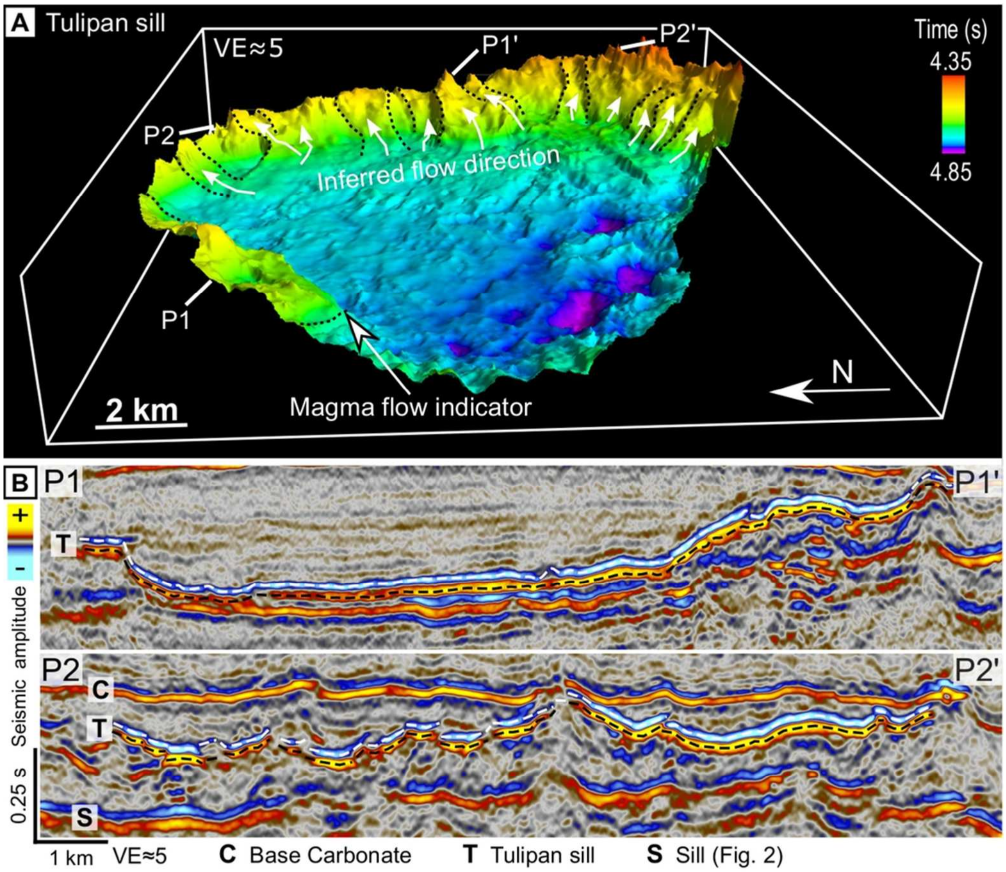

Figure 5: Seismic expression of the Tulipan sill. (A) 3D visualization of the saucer-shaped geometry of the top Tulipan sill horizon. Radial magma flow indicators mark edges of reflection segments representing upward, outward transgressing, igneous inclined sheets (Schofield et al., 2012b; Magee et al., 2014). (B) Seismic profiles show the cross-sectional expressions of the Tulipan sill (see (A) for location). P1 – P1' highlights the picked Tulipan sill top and base, whereas P2 – P2' visualizes the segmented character of the Tulipan sill reflection and indicates an underlying sill (S) below the Tulipan sill (Tulipan top - white dashed line; black dashed line tentatively interpreted as the sill base).

Figure 5

95x82mm (300 x 300 DPI)

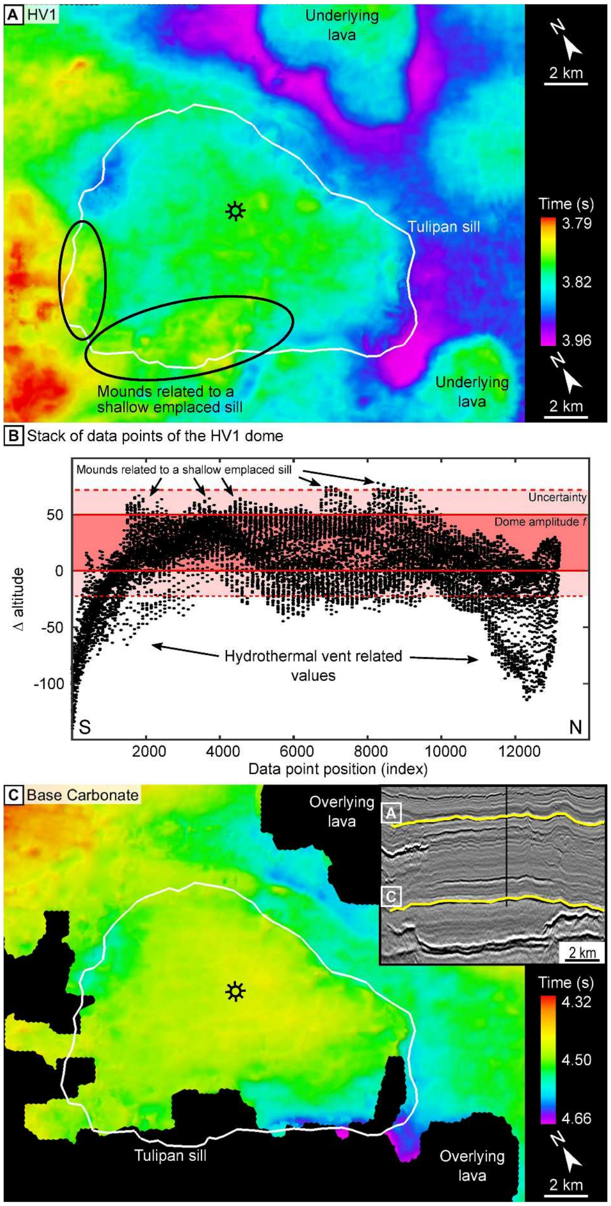

Figure 6: Time structure maps (two way travel time, TWT) and dome amplitude f. (A) HV1 time structure map shows the paleo-surface and top of the domed overburden during the emplacement of the Tulipan sill. (B) The stack of altitude data points within the Tulipan periphery highlights the plateau in the domed overburden. A best fit plane was used to estimate the base of the dome and calculate the amplitude f (red area). (C) Base Carbonate time structure map of the lowermost interpreted horizon above the Tulipan sill shows a good confined dome structure inside the Tulipan sill periphery. Subset shows the stratigraphic location of the (A) and (C).

Figure 6

218x431mm (300 x 300 DPI)

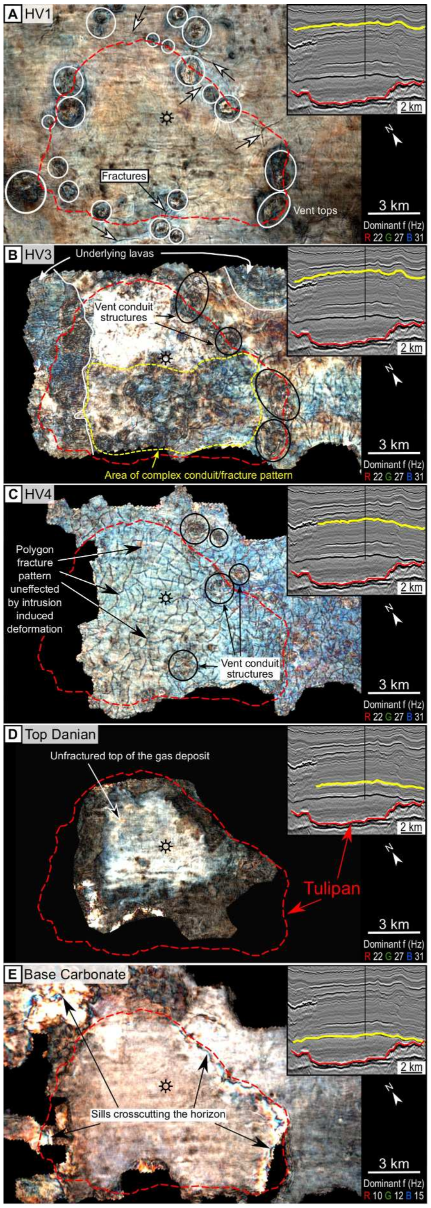

Figure 7: Spectral decomposition attributes maps of key horizons. Subsets display the same seismic section of Figure 3 (for location see Figure 2). The periphery of the Tulipan sill (red dashed line) corresponds to the map contour at the level of c. 4400 ms (TWT). (A) HV1 (Top Tang Formation) defines the top of the dome structure, and highlights hydrothermal vent complexes (HTVCs, white circles) and fractures in between (black/white arrows). (B) HTVCs on HV3 are obscured by lava flow pattern (outside the white lines). (C) HV4 envisages a regional polygonal fault system, and deeper parts of the HTVCs (black circles) identified in (A). (D) Top Danian shows no fractures in the top of the reservoir sandstones of the Tulipan prospect. (E) The Base Carbonate shows no evidence for central fractures, but highlights the crosscut of the underlying Tulipan sill. (The crosscut itself is not visible in the seismic subset).

Figure 7

240x678mm (300 x 300 DPI)

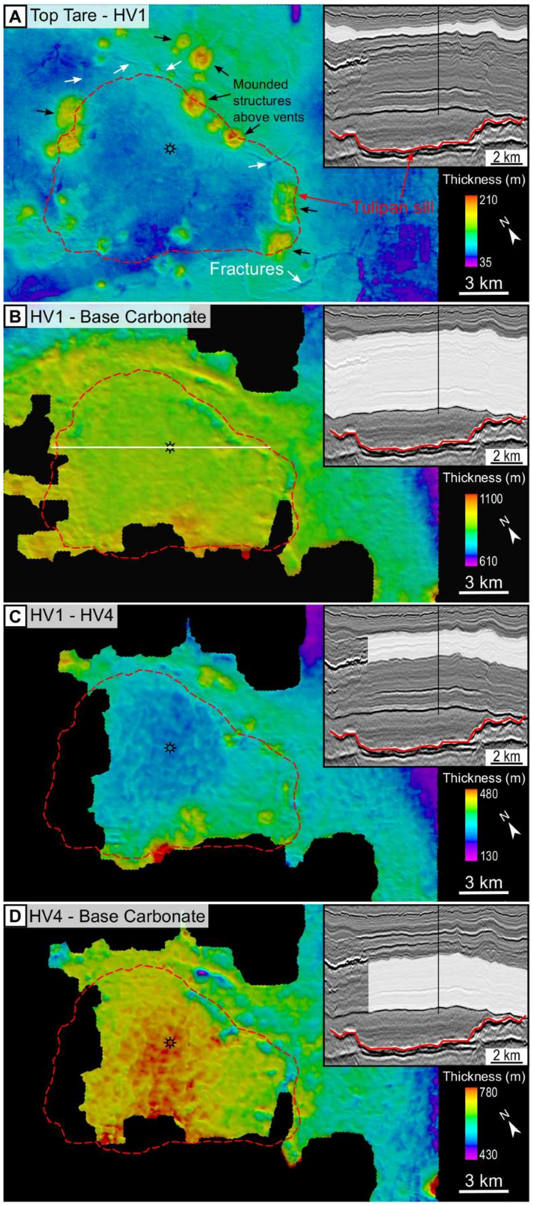

Figure 8: Thickness maps of the sedimentary sequences above the Tulipan sill. (A) Top Tare – HV1 isochron map shows the thickness anomalies (i.e. hydrothermal vent complex related mounds) in sedimentary strata right above the dome structure. (B) Isochron map of the complete strata interpreted (HV1 – Base Carbonate). White line shows the position of the seismic subset. (C) The upper dome structure, i.e. HV1 – HV4 isochron map, shows patchy thickness anomalies (thicker) in the close vicinity of the Tulipan sill periphery, whereas the central area is thin. (D) Isochron map of HV4 to Base Carbonate displays a contrasting thickness variation compared to (C) within the Tulipan sill periphery.

Figure 8

192x439mm (300 x 300 DPI)

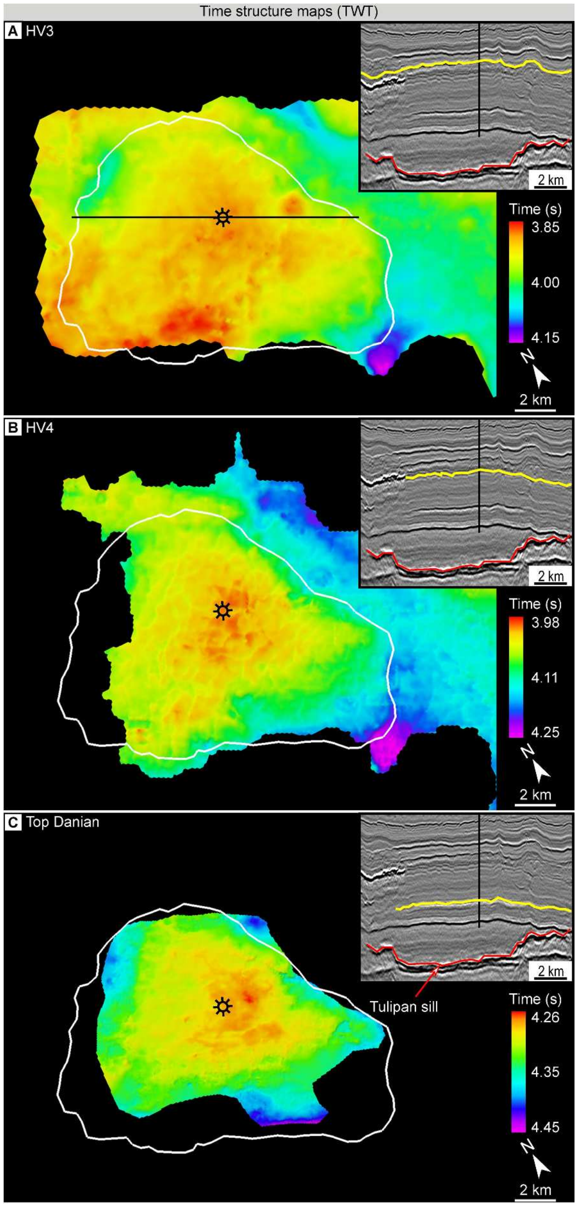

Supplemental material: Additional time structure maps
supplemental material
231x485mm (300 x 300 DPI)

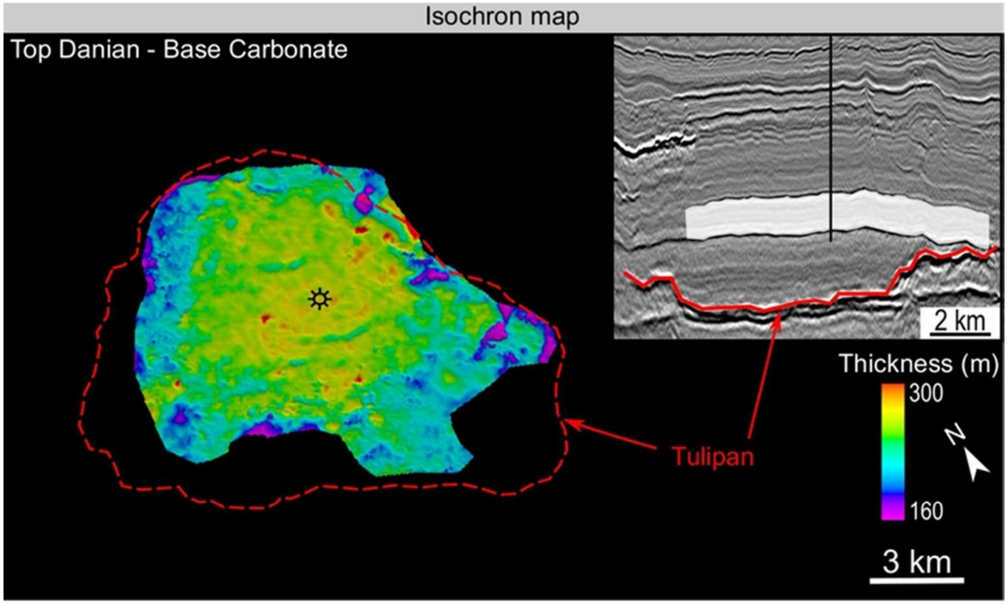

Supplemental material: Additional isochron map
supplemental material
66x39mm (300 x 300 DPI)

For Review